ACS APPLIED ELECTRONIC MATERIALS

pubs.acs.org/acsaelm Article

Quantitative Imaging of Defect Distributions in CdZnTe Wafers Using Combined Deep-Level Photothermal Spectroscopy, Photocarrier Radiometry, and Lock-In Carrierography

Alexander Melnikov, Andreas Mandelis,* Akshit Soral, Claudia Zavala-Lugo, and Michal Pawlak

Cite This: *ACS Appl. Electron. Mater.* 2021, 3, 2551−2563 Read Online

ACCESS | Metrics & More | Article Recommendations

ABSTRACT: Trap-state kinetic parameters were investigated in CdZnTe wafers using nondestructive and noncontacting deep-level photothermal spectroscopy (DLPTS), heterodyne photocarrier radiometry (HePCR), and lock-in carrierography (HeLIC) imaging. Two electronic carrier traps were found and activation energies were measured. Using a two-trap frequency-domain rate-equation theoretical model, full-wafer quantitative HeLIC images of recombination times, capture and emission coefficients, trap densities, and emission/capture relaxation times were reconstructed at 100 K. HeLIC imaging was used to discuss dynamic photocarrier interactions with CdZnTe traps. These quantitative images are very important in determining the optoelectronic behavior and the quality of CdZnTe substrate materials and fabricated devices, which is controlled by complex free-carrier density wave (CDW) and defect configuration interaction kinetic processes.

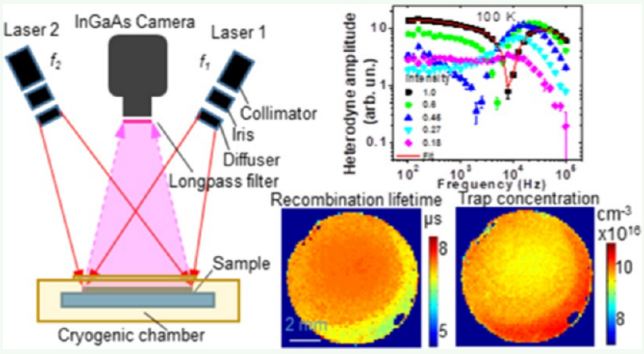

KEYWORDS: *CdZnTe, defect/trap density imaging, trap-state kinetic parameter imaging, heterodyne lock-in carrierography, deep-level photothermal spectroscopy*

1. INTRODUCTION

Rapidly growing applications of CdZnTe as a material suitable for X-ray and γ-ray detector fabrication[1−3] and for high-efficiency solar cells[4,5] have introduced the urgent need for characterization of photocarrier properties and their associated solid-state transport parameters, including their spatial distributions in wafer substrates, which affect charge transport and limit the performance of optoelectronic devices. Most popular diagnostic methods in use are current deep-level transient spectroscopy (I-DLTS), transient current technique (TCT), current and capacitance vs voltage ($I-V$ and $C-V$) measurements, γ-ray spectroscopy, Hall measurements, and optical and thermal measurements.[6−9] Beyond those methodologies, photocarrier radiometry (PCR) is a nondestructive and noncontacting spectrally gated frequency-domain dynamic semiconductor photoluminescence (PL) diagnostic modality, which allows for the simultaneous nondestructive determination of electronic transport parameters in semiconductor substrates and devices.[10−17] Subsequently, lock-in carrierography (LIC) was introduced as a near-infrared (NIR) imaging extension of PCR, aimed at constructing quantitative images of carrier transport parameters.[18−21] Next, two-beam heterodyne LIC (HeLIC) was introduced[22] to address the need for high-frequency photocarrier excitation, eliciting fast enough signal responses required to measure short recombination lifetimes and other fast photocarrier relaxation processes. HeLIC was developed to allow high-frequency dynamic imaging of optoelectronic material and device properties, which require sampling rates orders of magnitude higher than those achievable by the frame rates of today's fastest NIR camera technologies.[23−26] Very recently, heterodyne PCR (HePCR) proved to be very sensitive to photocarrier emission/capture processes out of, and into, band-gap defect and impurity states:[27] a newly discovered HePCR phenomenon[27] giving rise to a frequency-domain heterodyne signal amplitude depression ("dip" or "notch") accompanied by a 180° phase transition was attributed to a nonlinear kinetic mechanism of laser-excited harmonic carrier density waves (CDW) interacting with trap or defect states in Si wafers.[27] Important information about the number of trap/defect states involved in the carrier kinetics

Received: January 31, 2021
Accepted: May 24, 2021
Published: June 4, 2021

https://doi.org/10.1021/acsaelm.1c00100
ACS Appl. Electron. Mater. 2021, 3, 2551−2563

and the associated activation energies, which can be used to identify the physical origin of the trap states, can be obtained using deep-level photothermal spectroscopy (DLPTS).[28,29] The advantage of implementing DLPTS besides its noncontacting and nondestructive nature, as opposed to conventional electrical DLTS methods, is that of convenience as DLTPS may be easily and seamlessly integrated into the PCR and LIC instrumental setup.

In this paper, we report the appearance of the aforementioned notch phenomenon in the HeLIC pixel intermediate frequency responses of NIR InGaAs camera images of CdZnTe wafers exhibiting two band-gap traps/defects. Using a two-trap frequency-domain rate-equation theoretical model combined with DLPTS, HePCR, and HeLIC allowed the identification of photomodulated active CDW trap states and their spatial distributions. The notch phenomenon further allowed the unique unambiguous measurement of several optoelectronic parameters from a series of the HeLIC amplitude images obtained over a wide range of modulation frequencies, thereby enabling full-wafer-area quantitative HeLIC imaging of bulk recombination lifetimes, capture and emission coefficients (and relaxation times), and trap densities.

2. HELIC THEORY OF SEMICONDUCTORS WITH TWO BAND-GAP ELECTRONIC TRAP/DEFECT STATES

The nonlinear rate equations for p-type carrier kinetics (neglecting the minority n-type carriers for simplicity) in a semiconductor exhibiting two trap states (based on experimental evidence for our CdZnTe wafers, Section 4) can be written as[27]

$$\frac{dp(t)}{dt} = G(t) - \frac{p(t)}{\tau_p} - C_{p1}N_1(t)p(t) + e_{p1}[N_{T1} - N_1(t)] - C_{p2}N_2(t) + e_{p2}[N_{T2} - N_2(t)] \quad (1)$$

$$\frac{dN_1(t)}{dt} = -C_{p1}N_1(t)p(t) + e_{p1}[N_{T1} - N_1(t)] \quad (2)$$

$$\frac{dN_2(t)}{dt} = -C_{p2}N_2(t)p(t) + e_{p2}[N_{T2} - N_2(t)] \quad (3)$$

where $p(t)$ is the photogenerated free-hole carrier density, $G(t)$ is the optical generation rate, τ_p is the hole recombination lifetime, e_{p1} and e_{p2} are the thermal emission rates from traps 1 and 2, respectively, $N_1(t)$ and $N_2(t)$ are the trapped carrier densities in the two traps, respectively, C_{p1} and C_{p2} are the respective trap-state capture coefficients, and N_{T1} and N_{T2} are the corresponding trap densities.

Given that heterodyne excitation involves two optical excitation sources modulated at adjacent but different frequencies $f_1 = \omega_1/2\pi$ and $f_2 = \omega_2/2\pi$, both simultaneously incident on the semiconductor, the solution of eqs 1−3 can be expressed as a superposition of the various possible modulation modes as follows

$$G(t) = \sum_{m=-1}^{1} G_m e^{im\omega_1 t} + \sum_{n=-1}^{1} G_n e^{in\omega_2 t} \quad (4)$$

$$p(t) = \sum_{m=-1}^{1}\sum_{n=-1}^{1} p_{m,n} e^{i(m\omega_1 t + n\omega_2 t)} \quad (5)$$

$$N_1(t) = \sum_{m=-1}^{1}\sum_{n=-1}^{1} N_{1(m,n)} e^{i(m\omega_1 t + n\omega_2 t)} \quad (6)$$

$$N_2(t) = \sum_{m=-1}^{1}\sum_{n=-1}^{1} N_{2(m,n)} e^{i(m\omega_1 t + n\omega_2 t)} \quad (7)$$

Here, m and n indicate response harmonics for excitation at angular modulation frequencies ω_1 and ω_2, respectively. The solutions to eqs 1−3 can then be written as

$$p_0 = G_0\tau_p,\ N_{j(0,0)} = e_{pj}\tau_{3p}^{(j)}N_{Tj} \quad (8)$$

$$p_{10}(\omega_j) = \frac{G_0\tau_p}{(1 + i\omega_j\tau_p)\left[1 + \frac{i\omega_j\tau_p}{(1 + i\omega_j\tau_p)}\sum_{k=1}^{2} F_{k1}\right]} \quad (9)$$

$$N_j(\omega_k) = \frac{\tau_{3p}^{(j)}}{1 + i\omega_k\tau_{3p}^{(j)}}\left(e_{pj}N_{Tj} - \frac{p_{0,1}}{\tau_{2p}^{(j)}}\right) \quad (10)$$

$$F_{mn}(\omega_1) = \frac{\tau_{3p}^{(j)}}{(1 + i\omega_1\tau_{3p}^{(j)})\tau_{2p}^{(j)}},\ F_{nm}(\omega_2) = \frac{\tau_{3p}^{(j)}}{(1 + i\omega_2\tau_{3p}^{(j)})\tau_{2p}^{(j)}} \quad (11)$$

The characteristic times are defined as

$$\tau_{2p}^{(j)} = \frac{1}{C_{pj}N_{j(0,0)}} \quad (12)$$

$$\tau_{3p}^{(j)} = \frac{1}{e_{pj} + C_{pj}p_0} \quad (13)$$

where $N_{j(0,1)}(\omega_1) \equiv N_j(\omega_1)$, $N_{j(0,1)}(\omega_2) \equiv N_j(\omega_2)$; j = 1,2. The frequency-domain signal is given by

$$\begin{aligned} S(\omega_1, \omega_2) = \sum_{j=-\infty}^{+\infty}\sum_{k=-\infty}^{+\infty} S_{j,k} e^{i(j\omega_1 + k\omega_2)t} \\ \propto \left[\sum_{j=-1}^{1}\sum_{k=-1}^{1} p_{j,k} e^{i(j\omega_1 t + k\omega_2 t)}\right] \\ \times \left[\sum_{j=-1}^{1}\sum_{k=-1}^{1} p_{j,k} e^{i(j\omega_1 t + k\omega_2 t)} + \sum_{j=-1}^{1}\sum_{k=-1}^{1} N_{1(j,k)} e^{i(j\omega_1 t + k\omega_2 t)} + \sum_{j=-1}^{1}\sum_{k=-1}^{1} N_{2(j,k)} e^{i(j\omega_1 t + k\omega_2 t)}\right] \end{aligned} \quad (14)$$

For heterodyne lock-in detection at the beat angular frequency $\Delta\omega = |\omega_1 - \omega_2|$, eq 13 yields the simplified form

$$\begin{aligned} S_{-1,1}(\Delta\omega) = [N_1(\omega_2) + N_2(\omega_2)]p_{1,0}^*(\omega_1) \\ + [N_1^*(\omega_1) + N_2^*(\omega_1)]p_{1,0}(\omega_2) \\ + 2p_{1,0}^*(\omega_1)p_{1,0}(\omega_2) \end{aligned} \quad (15)$$

https://doi.org/10.1021/acsaelm.1c00100
ACS Appl. Electron. Mater. 2021, 3, 2551−2563

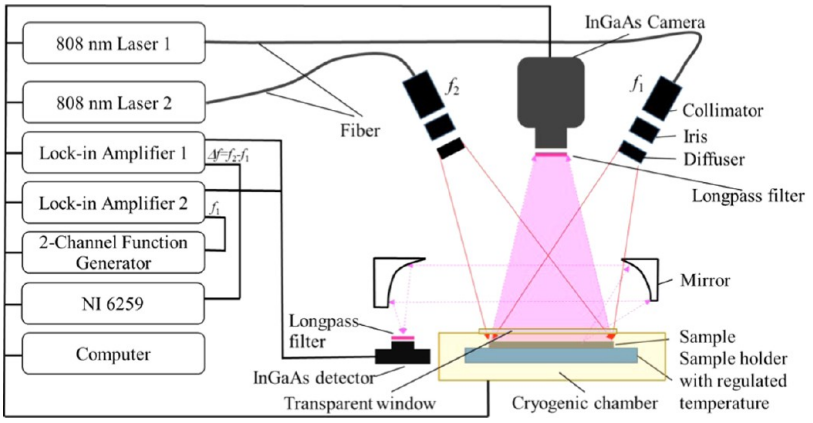

Figure 1. Schematic of heterodyne lock-in carrierography (HeLIC) combined with the homodyne ($f_1 = f_2$) and the heterodyne ($f_1 \neq f_2$) photocarrier radiometry (HePCR) setup.

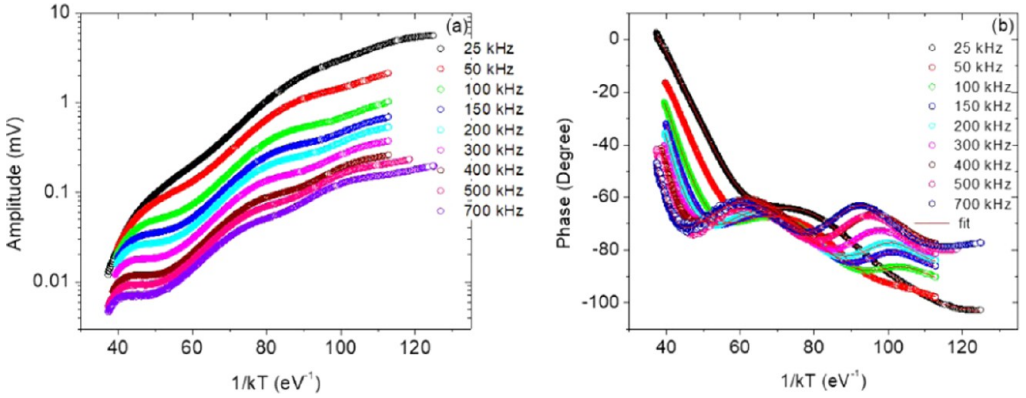

Figure 2. (a) Homodyne PCR amplitude and (b) homodyne phase of CdZnTe DLPTS dependencies on $1/kT$ at various laser-beam modulation frequencies.

3. EXPERIMENTAL SECTION

A schematic of the experimental PCR/HeLIC system is shown in Figure 1. In this system, the beams of two 808 nm fiber-coupled lasers were first collimated, then spread and homogenized by microlens arrays to form a 2 × 2 cm^2 illuminated area, consistent with the size of our CdZnTe wafers. Intensity changes were made by adjusting an iris placed in the path of each laser beam. The maximum intensity, I_{max}, was 1.9 W/cm^2 for each beam. The two beams for photoluminescence excitation were sine-wave modulated using a two-channel function generator in the range 0.1−700 kHz. The modulated radiative emissions from the sample were detected using a NIR InGaAs camera, model SU320KTSW-1.7RS170, from Goodrich Sensors Unlimited and an InGaAs detector, model PDA400. from Thorlabs. A long-pass filter LP-1000 nm from Spectrogon was used to prevent the excitation laser beams from interfering with the InGaAs NIR camera and the detector. Diffuse radiative recombination-induced signals were collected and collimated with two off-axis paraboloidal mirrors focused on the detector. The detected signal was demodulated using two lock-in amplifiers for the single-detector signal. In-house developed software was used for camera images referenced at the common frequency $f_1 = f_2$ in the case of homodyne LIC/PCR, and at the (beat) frequency difference $\Delta f = |f_1 - f_2|$ for heterodyne LIC/PCR. The frequency difference Δf between the two beams used in the HeLIC and HePCR measurements was 10 Hz for all experiments. Samples were placed on a Linkam LTS350 cryogenic stage, which allows maintaining a constant temperature in the −196 to +350 °C range and can provide temperature ramping.

$Cd_{0.9}Zn_{0.1}Te$ crystals were grown using the high-temperature and high-pressure vertical Bridgman−Stockbarger method.[8] Pure binary powders of CdTe and ZnTe (6N, Koch-Light), mixed together in a stoichiometric proportion, were placed inside a graphite crucible, kept at a temperature of about 1650 K for a few hours, and then the ingot was extracted from the heating zone at a speed of 2.4 mm/h. The extracted crystal rod was 1 cm in diameter and up to a few cm in length. Obtained ingots were sectioned with a wire saw perpendicular to the growth axis into about 1 mm thick slices (wafers), which were not oriented along any specific crystallographic plane. The wafers were polished and inspected with the scanning electron microscopy/energy-dispersive X-ray spectroscopy (SEM/EDS) method,[8] leading to the conclusion that the zinc content along the growth axis did not vary substantially among all crystals and, therefore, the segregation coefficient of zinc in the CdTe matrix was close to unity.

4. RESULTS, IMAGING, AND DISCUSSION

4.1. Deep-Level Photothermal Spectroscopy of Defect States in CdZnTe Wafers. The technique of deep-level photothermal spectroscopy (DLPTS)[28,29] was used for defect-state characterization of the samples. Typical homodyne PCR amplitude and phase temperature scans of our CdZnTe wafers at various frequencies are presented in Figure 2a,b, respectively. The amplitude temperature dependencies demonstrate several inflection points, whereas phase dependencies show strongly pronounced two peak/trough structures. These are evidence of the presence of at least two types of traps in CdZnTe. A correlation between local amplitude maxima superposed on a sloped background and phase peaks (smaller phase lags) with increasing temperature is evident at all frequencies, especially in the high-frequency range: trapped carrier thermal emission from trap or defect states contributes to increased free-carrier density at the band edge and leads to

https://doi.org/10.1021/acsaelm.1c00100
ACS Appl. Electron. Mater. 2021, 3, 2551−2563

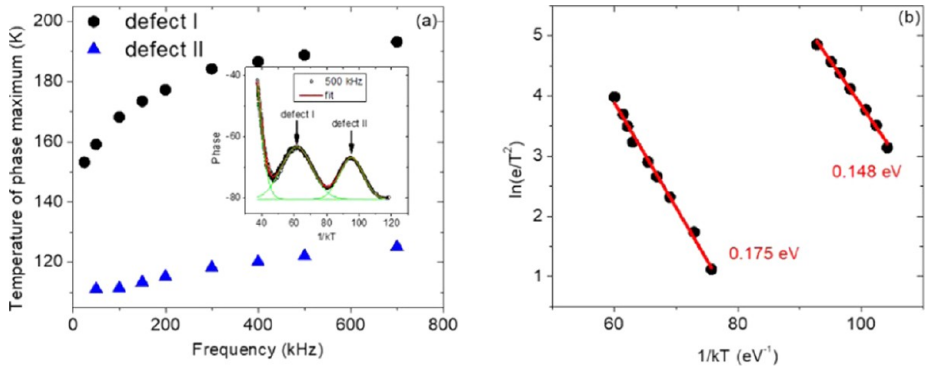

Figure 3. (a) Dependence of phase maximum temperature on frequency. The inset shows phase dependence on $1/kT$ at 500 kHz and best fits to Gaussian profiles. (b) PCR Arrhenius plots of e/T^2 for various frequencies and extracted activation energies.

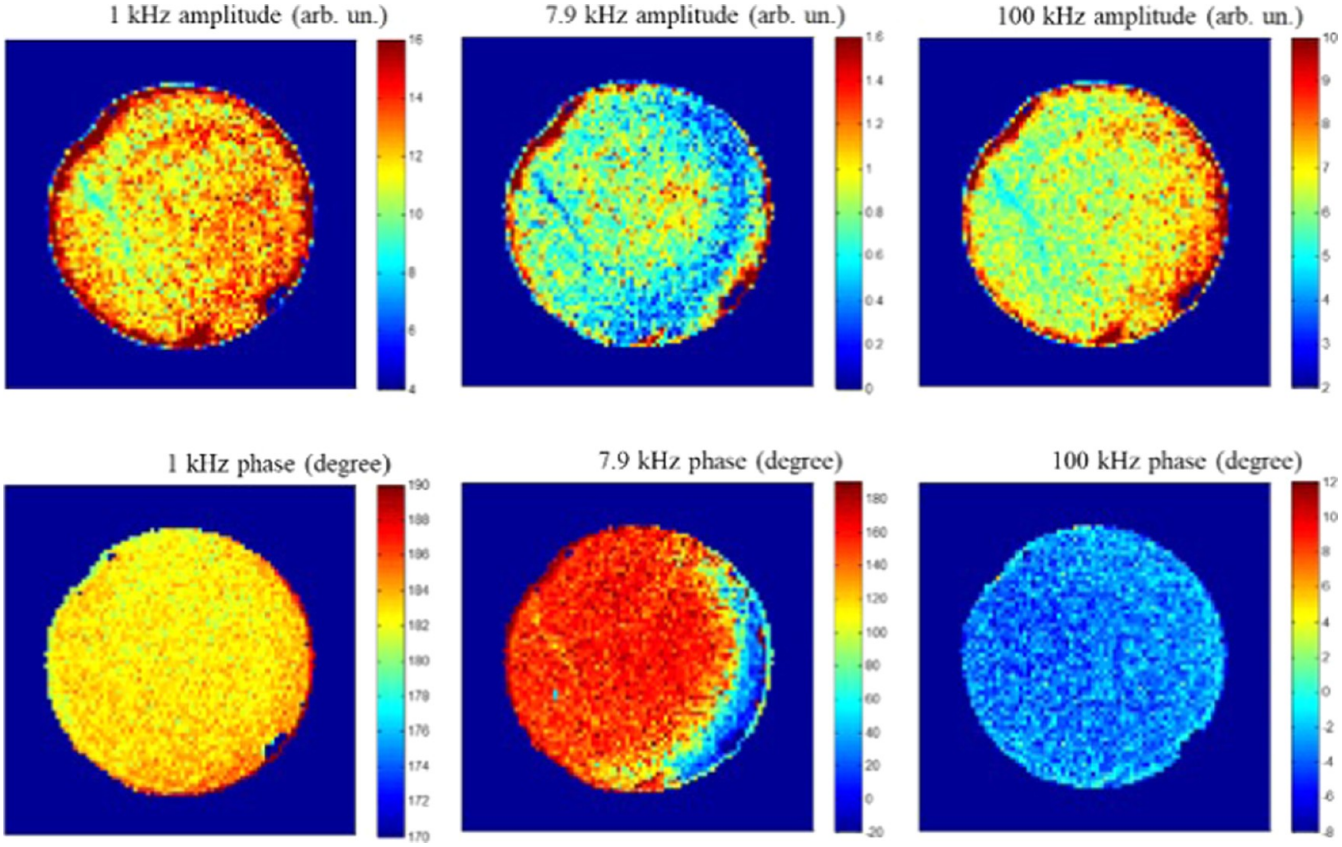

Figure 4. InGaAs camera HeLIC amplitude and phase images of CdZnTe at 1, 7.9, and 100 kHz at 100 K and intensity I_{max} (= 1.9 W/cm^2 for each beam).

enhanced PCR photon emission (photothermal) signal amplitude at decreased phase lag due to increased recombining photocarrier population near the wafer surface. The phase channel is preferable for analysis over the amplitude channel due to its higher contrast and sensitivity to the presence of electronic traps. The two phase peaks monotonically shifted to higher temperatures with increased modulation frequency, as shown in Figure 3a, consistent with the enhanced thermal emission rate observed in resonance with the modulated PCR signal from two band-gap traps or defects.[29,30] The phase dependencies on $1/kT$ were approximated by three Gaussian distributions, which allowed determining the precise temperature of the maximum for each peak. It should be mentioned that the three Gaussian best fits to the experimental photothermal phase spectra as functions of $1/kT$ were excellent at all frequencies, a sample of which at 500 kHz is shown in the inset of Figure 3a. The activation energy for thermal emission from the two defect or trap states was calculated through Arrhenius-plot fitting of the thermal emission rate, $e_n(T)$,[30] as shown in Figure 3b and described by[31]

$$e_n(T) = \gamma_n \sigma_n T^2 \exp\left(-\frac{E_a}{kT}\right) \tag{16}$$

where γ_n is a material constant, σ_n is the capture cross section by the deep level, and k is Boltzmann's constant. The thermal emission rate at each peak can be estimated by $e_n\ (T_{peak}) = 2.869\ \omega$,[28] where ω is the modulation angular frequency. The

https://doi.org/10.1021/acsaelm.1c00100
ACS Appl. Electron. Mater. 2021, 3, 2551−2563

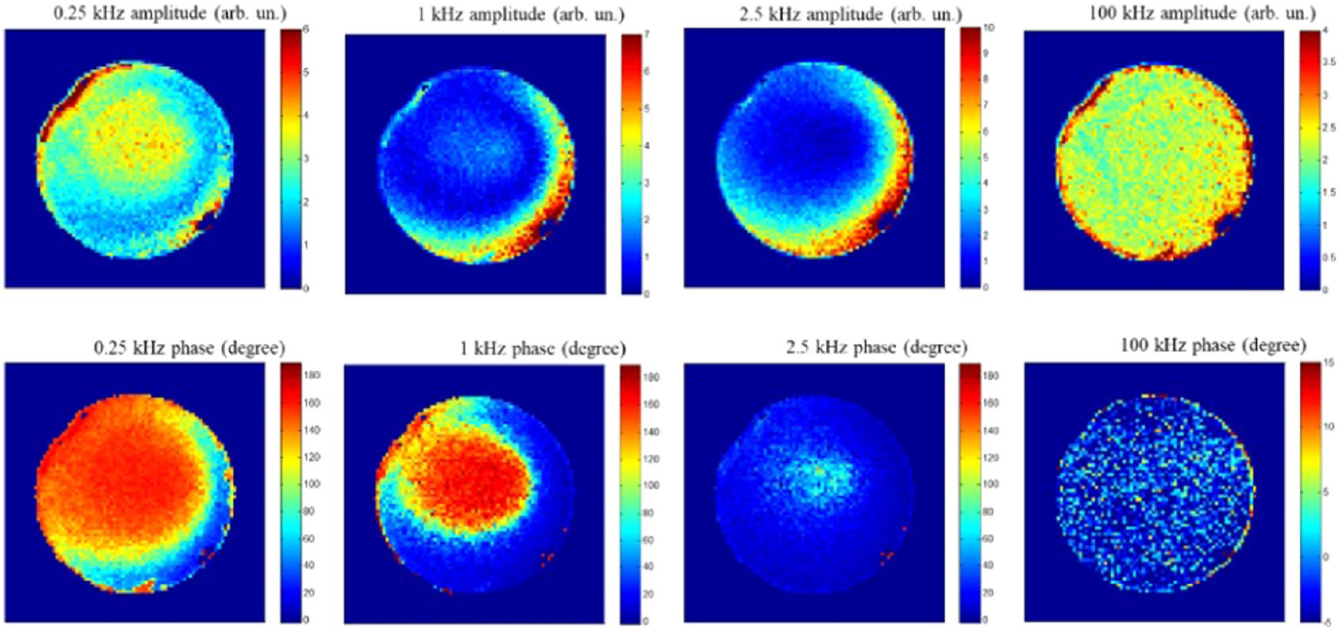

Figure 5. InGaAs camera HeLIC amplitude and phase images of CdZnTe at 0.25, 1, 2.5, and 100 kHz at 100 K and intensity 0.45 × I_{max}.

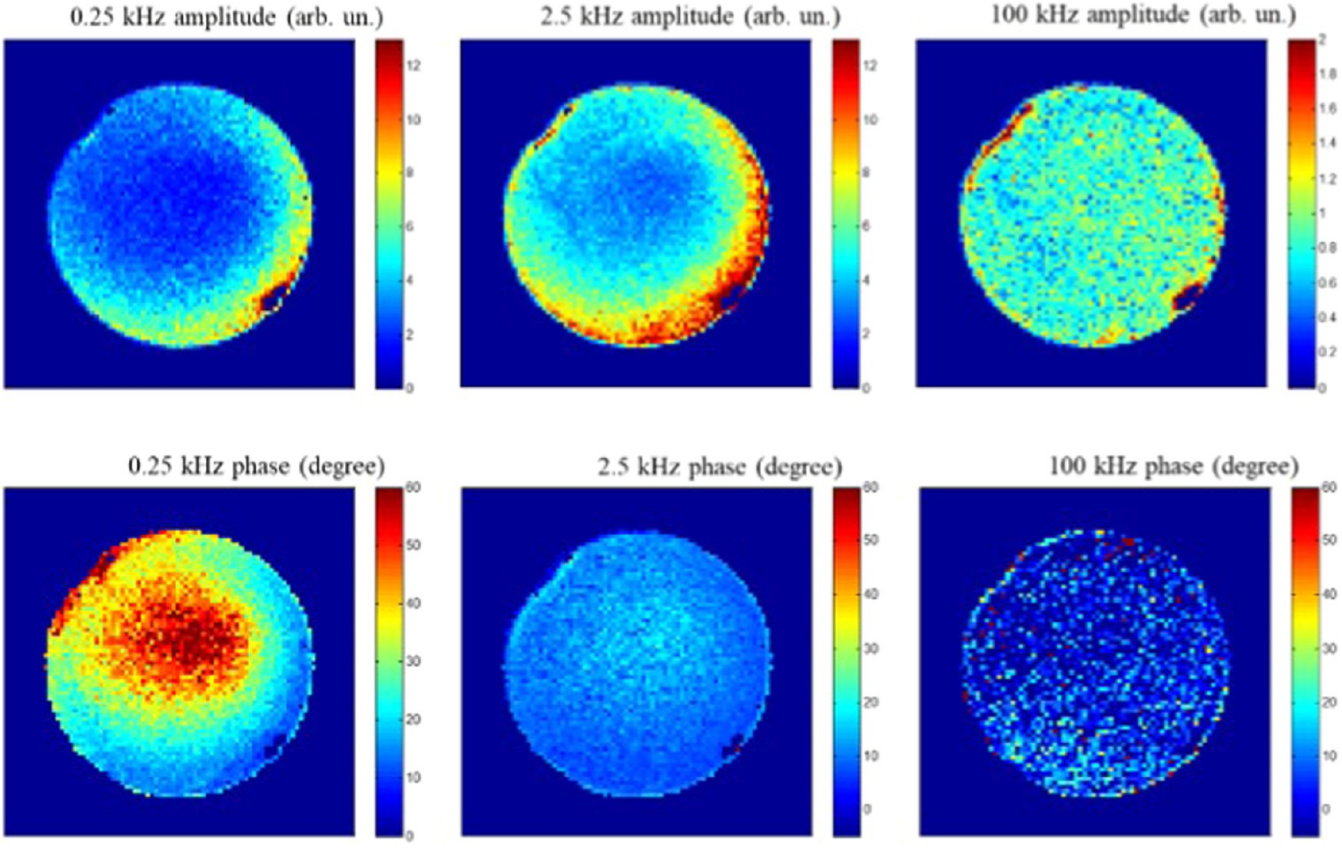

Figure 6. InGaAs camera HeLIC amplitude and phase images of CdZnTe at 0.25, 1, 2.5, and 100 kHz at 100 K and intensity 0.27 × I_{max}.

evaluated activation energies of two trap states were found to be 0.175 ± 0.005 and 0.148 ± 0.005 eV. The known ionization energies of the main intra-band-gap defects and impurities in $Cd_{1-x}Zn_xTe$[7] within the range of the activation energies shown in Figure 3b represent defects/traps comprising Cd native vacancies, V_{Cd}, in the 0.13−0.21 eV range, various acceptor impurity clusters in the 0.05−0.35 eV range, and pairing of Cd vacancies with a group III or group VII donor (designated as A centers), which are shallow acceptor complexes with a single ionization level. For A centers, the activation energy levels range from 0.12 to 0.15 eV. Castaldini et al.[32] used cathodoluminescence (CL), photoinduced current transient spectroscopy (PICTS) and photo-DLTS (P-DLTS) to identify more highly resolved activation energies of the A centers: the *A*

https://doi.org/10.1021/acsaelm.1c00100
ACS Appl. Electron. Mater. 2021, 3, 2551−2563

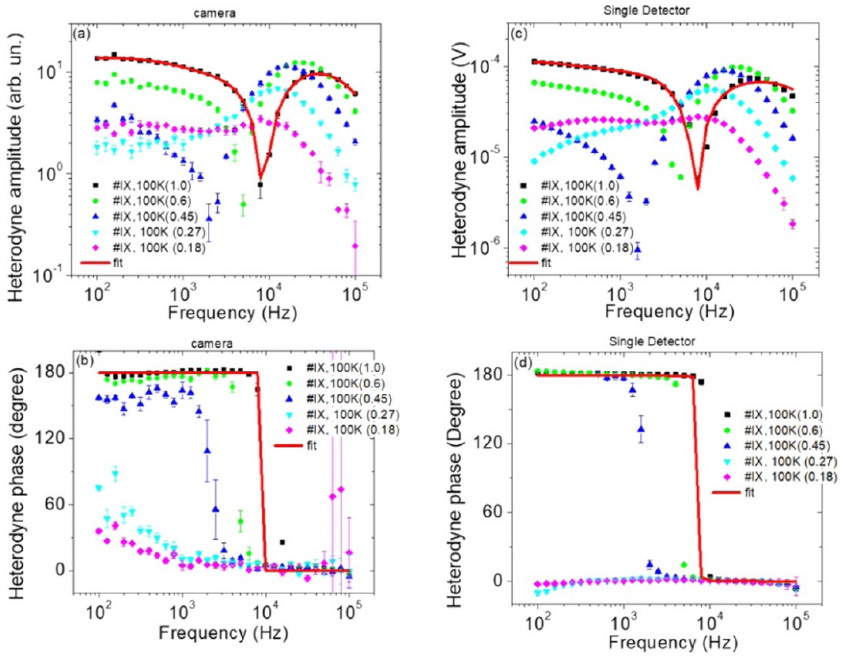

Figure 7. (a, b) Heterodyne amplitude and phase camera and (c, d) single-detector frequency scans of CdZnTe at 100 K for various intensities (described in the inset) from the same location. The mean values (averages) of four nearby pixels are shown.

level, E_v + 0.14 eV, and A_1 level, E_v + 0.15 eV, which have also been observed in PL investigations of CdZnTe[33] and are believed to be related to complexes involving a V_{Cd} and a V_{Te} vacancy, respectively. Very recently, a much more spectrally resolved study of thermally stimulated current peaks (TSC) from CdZnTe crystals[34] has attributed traps in the 0.154−0.159 eV range to dislocation-related defect complexes and traps in the range 0.174−0.179 eV to $O_{Te} - V_{Cd}^{-/2-}$ complexes. These authors identified the A center-associated traps lying in the 0.106−0.107 eV activation energy range, a different energetic location in the band gap from the earlier reports.

4.2. Heterodyne Lock-In Carrierography Imaging and HePCR of CdZnTe Wafers. Heterodyne lock-in carrierography (HeLIC) amplitude and phase images of CdZnTe wafers at various modulation frequencies and laser-beam intensities (I_{max}, 0.45 × I_{max}, and 0.27 × I_{max}) are shown in Figures 4−6, with the temperature of the sample kept at 100 K for an optimal signal-to-noise ratio (SNR). A heterodyne PCR amplitude depression (notch or dip) phenomenon recently observed in Si wafers with origins in destructive interference among trap-captured and -released carrier density waves due to the nonlinear nature of eqs 1−3[27] appeared in the HeLIC image pixel frequency response in the intermediate frequency range over the entire area of the sample around 7.9 kHz, at I = I_{max}, as shown in Figure 4. The phase images in Figure 4 exhibit values around 180° at low frequencies. As predicted by the carrier density wave theory of the frequency notch,[27] there is a sharp phase transition to ∼0° above the notch center minimum frequency in parts of the sample area in the intermediate frequency range. Above 7.9 kHz, the phase transition becomes complete throughout the entire sample area. Furthermore, as laser intensity decreases, the HeLIC amplitude notch center minimum shifts to lower frequencies: In the case of 0.45 × I_{max} intensity, as shown in Figure 5, phase switching starts from the sample edge at low modulation frequencies, spreads to the sample center region with increasing frequency, and phase transition (switching) occurs everywhere across the sample at high frequencies. A phase transition occurs at the frequency of the notch minimum amplitude and therefore it correlates with significant suppression of the HeLIC amplitude at that frequency. The phase images at low intensity (0.27 × I_{max}), as shown in Figure 6, demonstrate that transition has occurred below the minimum frequency measurement range and involves a significantly wider range above 0° due to sample inhomogeneity apparent at 0.25 kHz. At that frequency, the sample center exhibits a large phase lag (around 50−60°) accompanied by suppressed amplitude. This feature disappears with increasing frequency. Details of the heterodyne frequency behavior and its dependence on illumination intensity as expected from the nonlinear nature of eqs 1−3 and their solutions are shown in Figure 7. This figure shows and compares both camera HeLIC pixel frequency responses from a spot near the sample center and simultaneously measured single-detector HePCR frequency scans from the same location on the wafer at 100 K and several intensities. It is obvious that results from both measurements are very similar, despite the very different signal processing methods: using software for capturing low frame rate (around 100 Hz) camera heterodyne images and high-frequency (up to 10 MHz) hardware lock-in amplifier demodulation of the single InGaAs detector, respectively. The heterodyne amplitude frequency dependencies exhibit a very pronounced dip at the highest intensity I = I_{max}, as shown in Figure 7a,c, accompanied by ∼180° phase transition, as shown in Figure 7b,d. The dip shifts to lower frequencies with decreasing illumination intensities and is inferred to lie below the measured frequency range at low intensities, I < 0.45 I_{max}.

4.3. Quantitative Dynamic and Kinetic Parameter HeLIC Imaging of Entire CdZnTe Wafers. The theory presented in Section 2 was used to fit the HeLIC frequency response data of the camera pixels and the single-detector HePCR data, as shown in Figure 7. The frequency depend-

https://doi.org/10.1021/acsaelm.1c00100
ACS Appl. Electron. Mater. 2021, 3, 2551−2563

encies of both methods are almost identical. The parameters, τ_p, C_{p1}, e_{p1}, C_{p2}, e_{p2}, N_{T1}, and N_{T2}, were evaluated from the best fits to data for maximum illumination intensity according to the two-trap theoretical model, and the results are shown in Table 1. The fminsearchbnd solver[35] was used to minimize the sum of the squares of errors between the experimental and calculated data starting with random initial values of fitting parameters within a fixed interval. Different starting points delivered different results of the theoretical curve best-fitted to the experimental points. In this manner, the mean values of the foregoing parameters and their standard deviations, a measure of the scatter of the best-fitted results, were determined. Furthermore, the standard deviations show the accuracy/uniqueness of the fitted parameters. These numbers were found to be very close and showed consistency between the two methodologies. Conversely, the absence of a well-defined notch increases the standard deviation and compromises measurement uniqueness by increasing standard deviations. The evaluated parameters shown in Table 1 also have very similar values. The recombination time, τ_p, measurements demonstrate very high reliability and negligible standard deviations, while some other parameters show relatively higher standard deviations. This may be caused by the limited number of experimental points and/or the compounded error of multiple measured primary parameters used in the calculation of secondary parameters. The evaluated recombination lifetime is close to the literature reported hole lifetime of 2.5 μs in Redlen HF CdZnTe.[36] In summary, it is important to mention that, as a general rule, the presence of an amplitude frequency notch phenomenon accompanied by a phase transition renders the carrier kinetic parameter measurements precise and unique with values characterized by low standard deviations.

Table 1. Optoelectronic Parameters Evaluated from Camera Heterodyne Amplitude and Phase and Single-Detector Frequency Scans of CdZnTe at 100 K for Max Intensity I_{max}

parameter	camera HeLIC	single-detector HePCR
τ_p (μs)	2.02 ± 0.00	1.96 ± 0.00
C_{p1} (cm^3/s)	(2.3 ± 1.2) × 10^{-12}	(3.2 ± 2.7) × 10^{-12}
e_{p1} (s^{-1})	(7.66 ± 0.04) × 10^4	(7.2 ± 0.1) × 10^4
C_{p2} (cm^3/s)	(3.3 ± 2.4) × 10^{-13}	(3.4 ± 2.5) × 10^{-13}
e_{p2} (s^{-1})	(5.03 ± 0.08) × 10^3	(4.18 ± 0.08) × 10^3
N_{T1} (cm^{-3})	(7.0 ± 4.1) × 10^{16}	(8.1 ± 6.8) × 10^{16}
N_{T2} (cm^{-3})	(5.5 ± 3.5) × 10^{15}	(4.4 ± 2.7) × 10^{15}

Figure 8 depicts quantitative recombination lifetime images for intensities, I_{max}, 0.45 × I_{max} and 0.27 × I_{max} with the corresponding recombination lifetime profiles across the sample horizontal diameter and the heterodyne frequency dependencies of four chosen pixels. The central region of the sample is characterized by small recombination lifetimes, which increase near the rim. The differences between the center and the rim are enhanced with decreasing excitation intensity. Furthermore, a general trend for increasing lifetime with decreasing intensity is observed in the three images, an effect typically attributed to trap occupancy increase in the presence of fewer excitation photons, thereby decreasing the probability of free-carrier capture resulting in increasing statistical

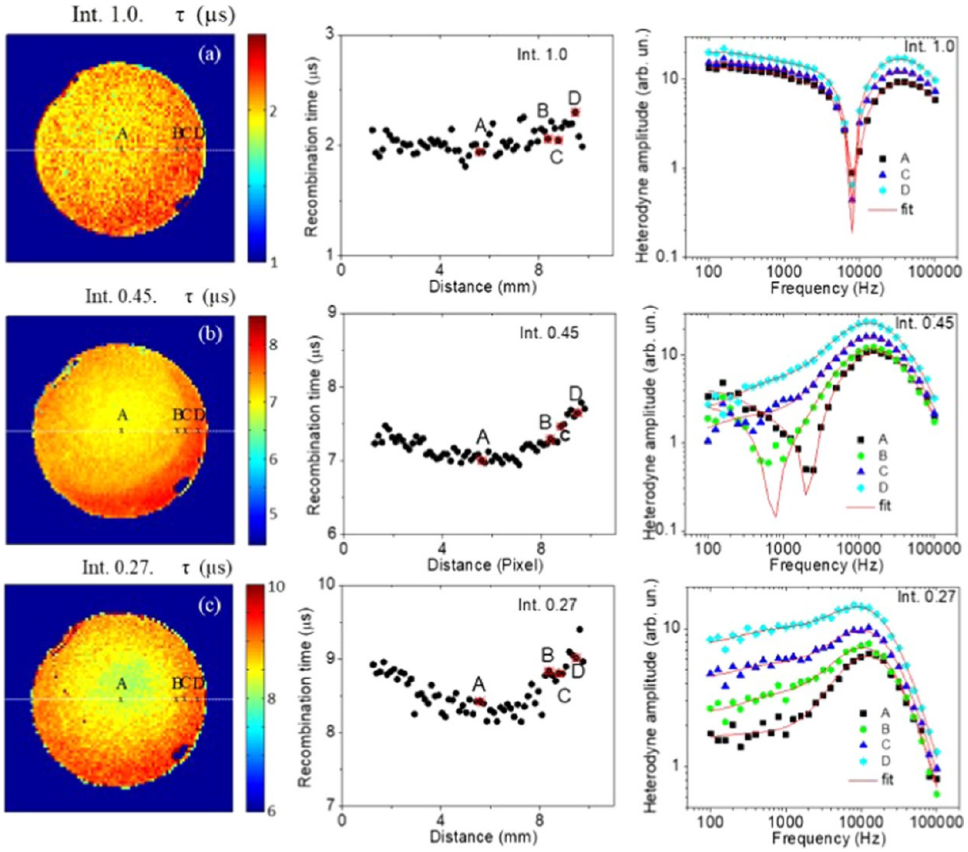

Figure 8. Quantitative recombination lifetime images of CdZnTe at 100 K for relative intensities 1.0 (a), 0.45 (b), and 0.27 (c) with corresponding recombination lifetime profiles across the horizontal diameter (dashed line) and HeLIC pixel amplitude frequency scans for points A, B, C, and D.

https://doi.org/10.1021/acsaelm.1c00100
ACS Appl. Electron. Mater. 2021, 3, 2551−2563

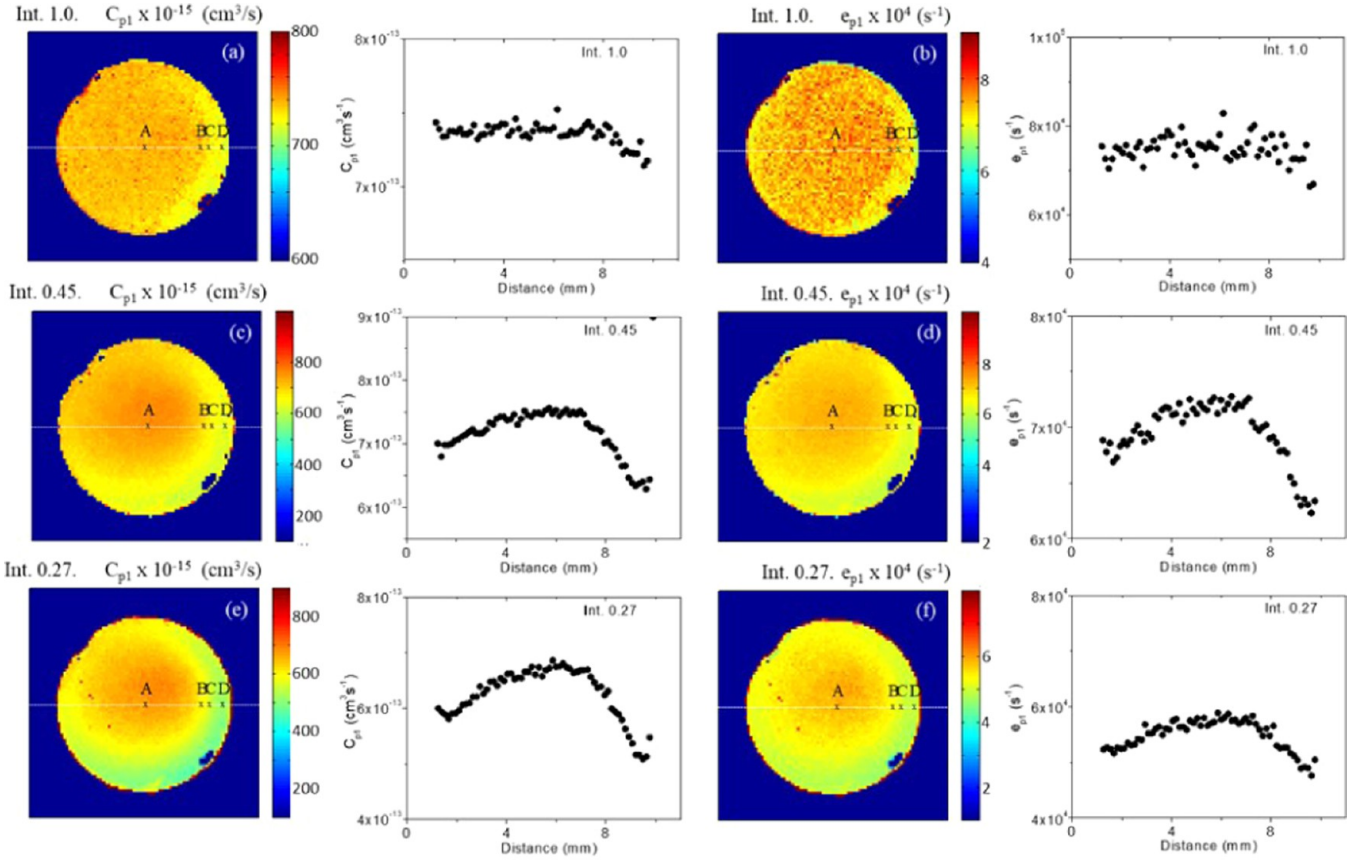

Figure 9. Quantitative capture coefficient (a, c, e) and emission rate (b, d, f) images of defect/trap #1 at 100 K with corresponding profiles across the horizontal diameter (dashed line) for relative intensities 1.0 (a, b), 0.45 (c, d), and 0.27 (e, f).

recombination lifetime. The HeLIC frequency scan at I_{max} exhibits a very sharp notch with a fixed frequency position along all four sample diameter points A, B, C, and D. For the intermediate intensity, however, the notch full-width at half-maximum (FWHM) broadens, with the minimum shifting to distinct frequencies for each pixel and disappearing altogether with increasing lifetime at location D near the sample rim. The low-intensity frequency scans show only very broad amplitude valleys at low frequencies with no notch presence. A major feature of the HeLIC signal is that it is very sensitive to capture/emission/recombination processes that involve trap parameters through the rate equations: the emission rate and capture coefficient and trap density, leading to significant changes of HeLIC frequency scans for different wafer locations and beam intensities.

Figure 9 shows the derived quantitative capture coefficient and thermal emission rate images of defect/trap #1 and the corresponding cross-diameter profiles for the same intensities, as shown in Figure 8. The central part of the sample is characterized by a lower emission rate and capture coefficients than the crescent-like region near the rim. Decreasing intensity makes these differences more pronounced. Lower emission rates in the crescent region may result in higher trap occupancy and thus longer recombination lifetimes, consistent with the increased lifetime distribution images in that region, as shown in Figure 8. This is also consistent with the lower trapping rate distribution image, as shown in Figure 9e.

Figure 10 shows quantitative capture coefficient and emission rate images of defect/trap #2 and the corresponding cross-diameter profiles for the same intensities, as shown in Figures 8 and 9. The behavior of these parameters at intensity I_{max} is similar to that of trap #1. Here, decreasing intensity leads to the appearance of a transition region between the central and crescent regions already identified in the images of trap #1: points B and C belong to this region at intermediate intensity, whereas point A at the center belongs to the transition region at low intensity. Heterodyne frequency scans show strong suppression of amplitude along the transition region with high levels of noise over a wide low-frequency range and the absence of a pronounced notch. As a result, the reliability of fitted parameters of trap #2 in the region is low, also because the smaller concentrations of the defect increase the standard deviation of the quantitative C_{p2} and e_{p2} images.

Figure 11 shows quantitative images of both trap densities N_{T1} and N_{T2}. From a practical viewpoint, these images are of key importance for the nondestructive and noncontacting evaluation of the degree of (opto)electronic integrity, uniformity, and quality of the semiconductor materials under consideration and their suitability as substrates for photonic device fabrication. Inhomogeneous distributions of both trap states are observed in the sample with higher densities in the central region than near the rim. It is clear that the density of trap #1 is higher than that of trap #2 over the entire sample. This distribution difference is consistent with the respective relative emission/capture distributions from/into trap #2 and the emission/capture images shown in Figure 10. For the latter trap, the transition region at intermediate and low laser intensities shows anomalous values of N_{T2}, which may not be entirely reliable due to its much lower density map than that of N_{T1}. From the images in Figure 11, it is clear that the crescent-

https://doi.org/10.1021/acsaelm.1c00100
ACS Appl. Electron. Mater. 2021, 3, 2551−2563

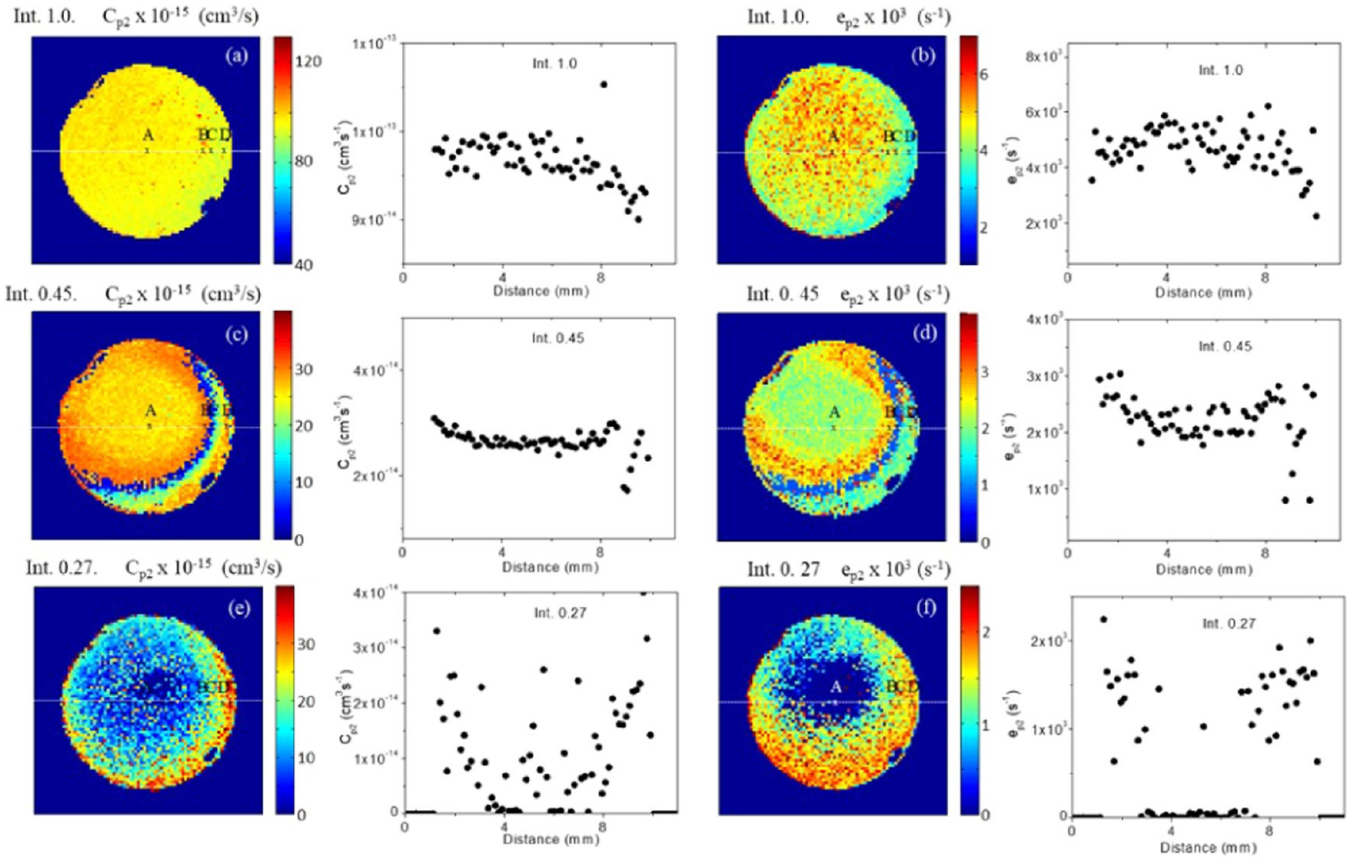

Figure 10. Quantitative capture coefficient (a, c, e) and emission rate (b, d, f) images of defect/trap #2 at 100 K with corresponding profiles across the horizontal diameter (dashed line) for relative intensities 1.0 (a, b), 0.45 (c, d), and 0.27 (e, f).

shaped region on the right side has lower trap densities than the remaining regions of the wafer, a fact that is consistent with the higher recombination lifetime images shown in Figure 8 in that region. The calculated trap densities N_{T1} are on the order of 10^{16}−10^{17} cm^{-3} and those for N_{T2} are on the order of 2.0×10^{15}−1.5×10^{16} cm^{-3}. The quantitative trap density images are outcomes of the theoretical model of eqs 1−3, which describes a general two-trap system consistent with the DLPTS data shown in Figures 2 and 3. While the N_{T2} trap densities are generally in agreement with activation energies in the 0.10−0.18 eV range, which have been reported to be $\sim(1.23-8) \times 10^{15}$ cm^{-3},[6,34,37] those of the N_{T1} densities are on the high side, or higher than, published deep-level trap densities in $Cd_{1-x}Zn_xTe$. There are three possible explanations for the possibility of measuring higher than expected trap densities: (1) The known ionization energies of the main intra-band-gap defects and impurities in $Cd_{1-x}Zn_xTe$[7] within the range of the activation energies shown in Figure 3b represent defects/traps comprising Cd native vacancies, V_{Cd}, in the 0.13−0.21 eV range, various acceptor impurity clusters in the 0.05−0.35 eV range, and pairing of Cd vacancies with a group III or group VII donor (designated as A centers), which are shallow acceptor complexes with a single ionization level. The proximity of these energetically adjacent defect cluster states is such that thermal energetic overlap cannot be excluded in our DLPTS measurements, which thus may have led to increased effective trap densities when evaluated by the kinetic model of eqs 1−3. This possibility suggests carrying out more highly resolved temperature thermal scans to identity overlapped adjacent peaks.[34] (2) In the context of the highly nonequilibrium steady-state heterodyne optical excitation, with large fluctuating numbers of free excess carriers roaming at, or near, the band edge, impurity states emptied by the laser beam modulated at one frequency may act as extra traps of free carriers generated by the other, phase lagged, laser beam, thereby rendering the effective trap densities N_{T1} and N_{T2} functions of time. This possibility was considered in the detailed theory of HePCR trap-state kinetics of p-type Si[27] and was found to be consistent with the observed notch phenomenon at the minimum-amplitude (resonant) laser modulation frequencies at which the trap optical excitation/emission rate equals the trapping rate. (3) A third possibility is due to the absence of a CDW diffusion mechanism from the nonlinear kinetic model of eqs 1−3 for simplicity: The number densities of free CDW measured in this model as spatially stationary are smaller than the actual densities because an unaccounted fraction of free carriers diffuses away from the location of the detector. Therefore, the effective smaller free CDW calculated under the spatially stationary assumption will have to be associated with more trap states under dynamic steady-state kinetics, i.e., with higher effective trap densities. In any of these three possible mechanisms, the effective trap densities measured using the CDW rate equations with the data from the HeLIC imaging technique and/or HePCR may be higher than the actual native trap concentrations. This, however, is a conclusion that can affect the quantitative trap map densities but not their relative distributions across the optoelectronic material volumes. The importance of quantitative trap density images lies in the fact that these densities and their distributions under optical excitation conditions control

https://doi.org/10.1021/acsaelm.1c00100
ACS Appl. Electron. Mater. 2021, 3, 2551−2563

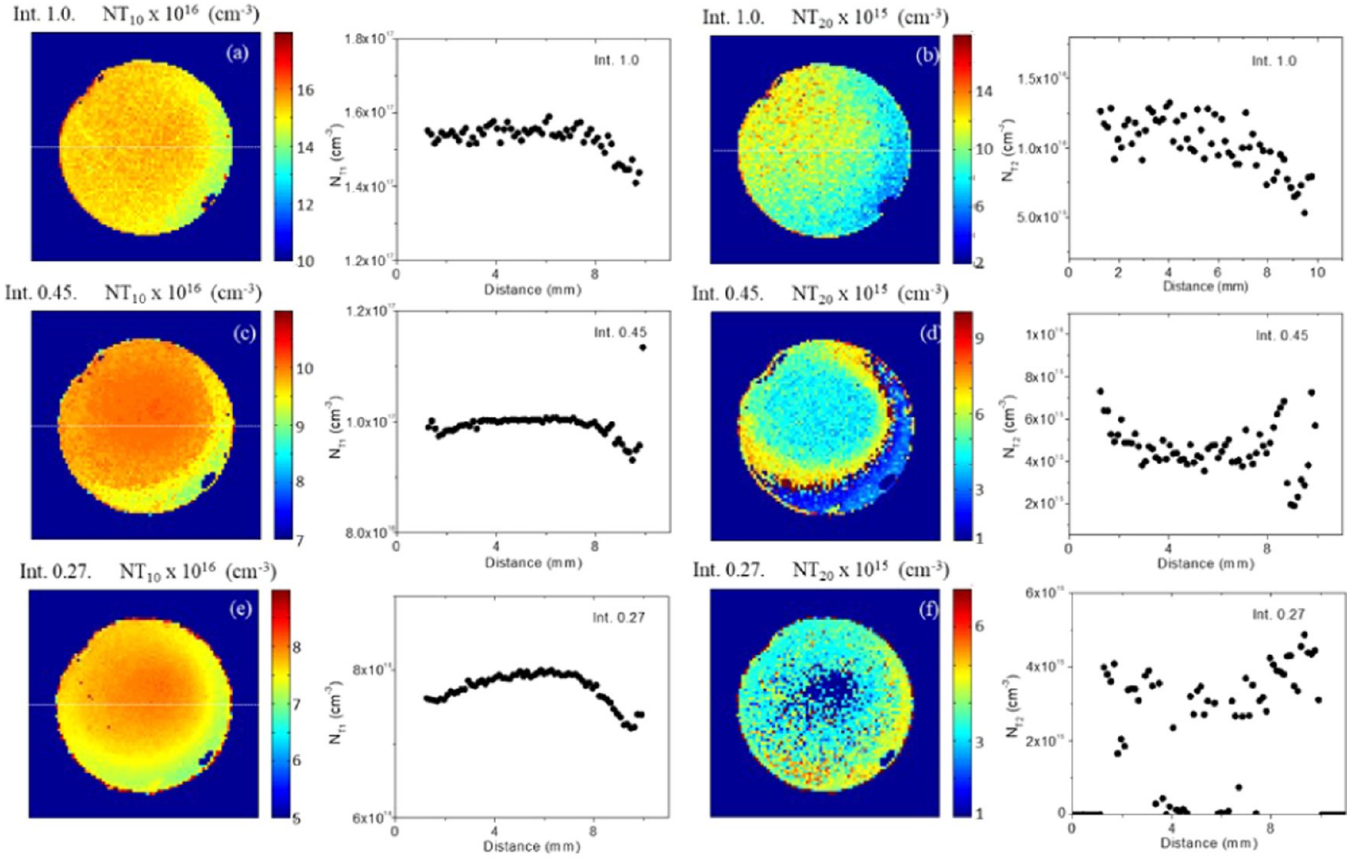

Figure 11. Quantitative density of the trap #1 (a, c, e) and of trap #2 (b, d, f) images at 100 K, and corresponding profiles along the horizontal diameter (dashed line) for relative intensities 1.0 (a, b), 0.45 (c, d), and 0.27 (e, f).

the CdZnTe optoelectronic behavior and properties when this material is used as a substrate for radiation detectors[38] and high-efficiency solar cells.[4,5] In our measurements, the values of N_{T1} and N_{T2} calculated in the mappings of Figure 11, also consistent with HePCR measurements, Table 1, were found to be consistent with conventional homodyne PCR measurements.[10] This agreement implies that possibility #2 must be discarded, while possibility #1 may be the most likely cause due to adjacent trap overlaps in the 0.05−0.35 eV intra-band-gap range for N_{T1}, while the other, more isolated N_{T2} defect state in the 0.10−0.18 eV range, represented by the HeLIC images, are likely to yield accurate trap densities, also in agreement with literature values.[6,34,37] A study of trap densities from HeLIC imaging and the underlying mechanism for the possibility of overestimation is currently under further investigation using CdZnTe crystals with known defect concentrations as validation standards.

4.4. Alternative Quantitative Multirelaxation Lifetime Imaging of Entire CdZnTe Wafers. Along with the kinetic optoelectronic quantities, e_{pj}, C_{pj}, and N_{Tj}, derived grouped parameters such as relaxation times $\tau_{2p}^{(j)}$ and $\tau_{3p}^{(j)}$, eqs 12 and 13, can be imaged and used for the characterization of entire CdZnTe wafers. $\tau_{2p}^{(j)}$ is sensitive to the capture rate and the trap concentration, while $\tau_{3p}^{(j)}$ also involves the trap emission rate. These relaxation times were calculated on the basis of best-fitted τ_p, C_{p1}, e_{p1}, C_{p2}, e_{p2}, N_{T1}, and N_{T2} according to eqs 8−11 and 14. Relaxation time images at various intensities are shown in Figure 12. Lower emission and trapping rates are consistent with longer emission and trapping lifetimes as demonstrated here. These relaxation time images clearly highlight the sample inhomogeneities under a common unit (time) and make it easier to compare the effects of the foregoing material kinetic quantities. In Figure 12, under high relative laser-beam intensities, the central region exhibits shorter $\tau_{2p}^{(j)}$and $\tau_{3p}^{(j)}$, j = 1,2, than the crescent on the right side, and the same is true for the entire near-rim region overall. However, the relaxation time images for the trap/defect #2 at intermediate and low intensities reverse this trend and appear to support longer relaxation times within the central region. This is consistent with the distributions of emission rates from that trap in those regions, as shown in Figure 10b,d,f.

Figure 13 shows relaxation times along with trap densities N_{Tj}, j = 1,2, emission rates, e_{pj}, capture coefficients, C_{pj}, and relaxation times, τ_p,$\tau_{2p}^{(j)}$, $\tau_{3p}^{(j)}$ and their dependencies on relative intensity for the two traps/defects at the center of the sample (point A). Increasing intensity results in increasing trap concentration N_{Tj}, consistent with decreased occupancy due to increased emission rates, e_{pj}, of trapped carriers, as expected, while the capture rate remains relatively flat for both trap distributions. The derived relaxation times, including the recombination lifetime, decrease proportionately with increasing intensity and N_{Tj}, e_{pj}, as expected from the higher vacant trap availability.

5. CONCLUSIONS

Heterodyne lock-in carrierography was successful employed for nondestructive quantiative distribution imaging of defect/trap densities and relevant kinetic CDW parameters in CdZnTe. The heterodyne amplitude frequency scans were found to be characterized by the presence of a recently discovered notch

https://doi.org/10.1021/acsaelm.1c00100
ACS Appl. Electron. Mater. 2021, 3, 2551−2563

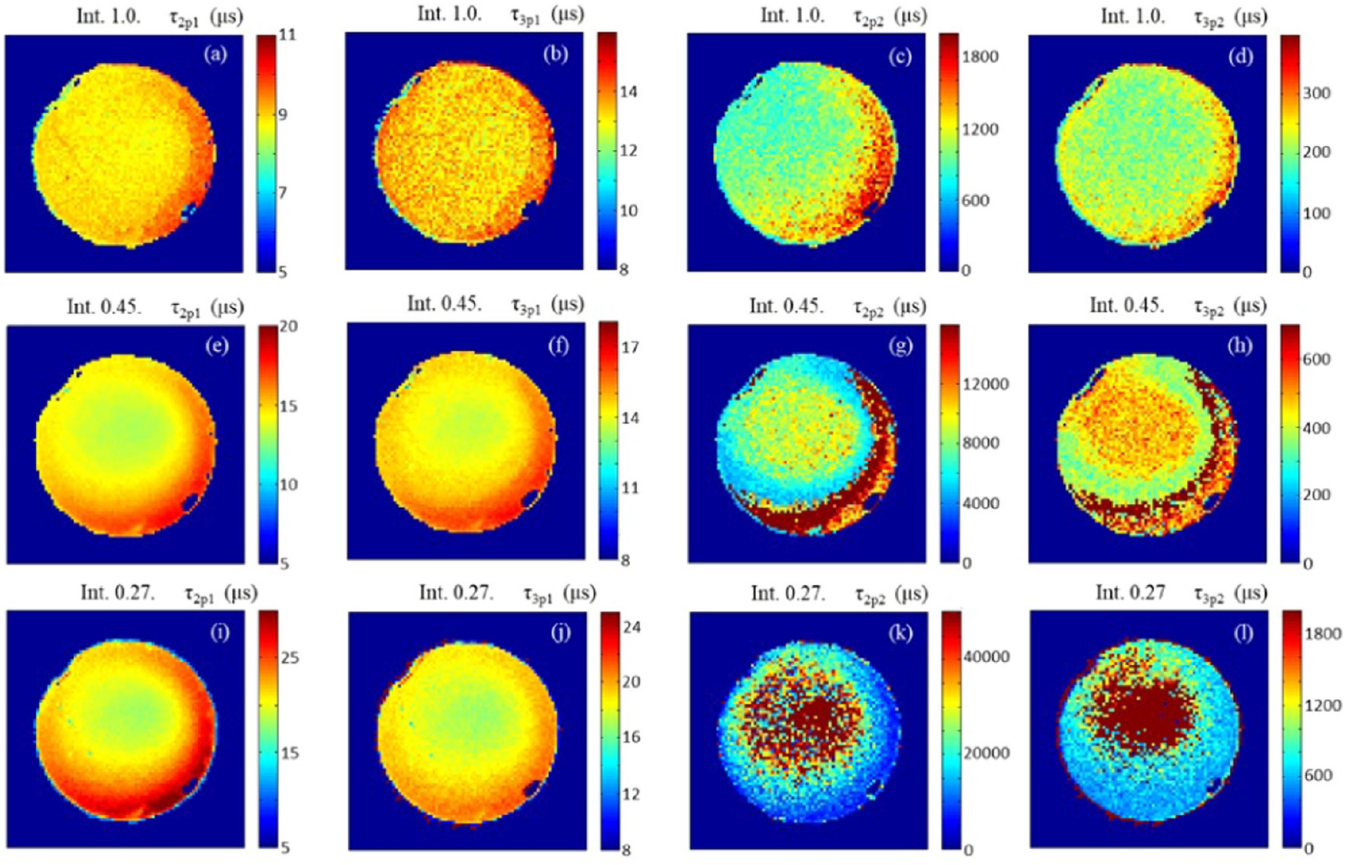

Figure 12. Multirelaxation time τ_{2p1} (a, e, i), τ_{3p1} (b, f, j), τ_{2p2} (c, g, k), and τ_{3p2} (d, h, l) images derived from τ_p, C_{pj}, e_{pj}, and N_{Tj} images and eqs 12 and 13 at 100 K for relative intensities 1.0 (a, b, c, d), 0.45 (e, f, g, h), and 0.27 (i, j, k, l).

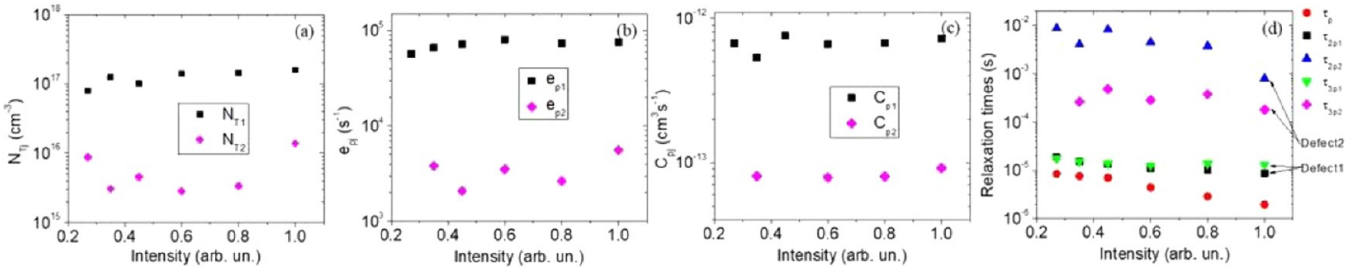

Figure 13. Two-trap concentrations (a), emission rates (b), capture coefficients (c), and relaxation times (d) as functions of laser-beam intensity at 100 K for point A.

(dip), the frequency position of which depends on excitation laser intensity and location of the sample. Two band-gap traps were found with energy activation 0.148 and 0.175 eV using photothermal spectroscopy. The spatial distribution images of parameters such as recombination lifetime, capture coefficients, emission rates, and concentrations of both traps were evaluated on the basis of a theoretical dynamic nonlinear rate-equation model with two band-gap traps. As alternative imaging parameters, images of the trap capture and emission characteristic times were obtained for the two trap states. The combination of DLTPS and HeLIC imaging yielded inhomogeneous distributions/surface maps of the aforementioned parameters in CdZnTe wafers with large variations from the center to the edge. It was shown that HeLIC imaging can be effectively used to determine the kinetic properties of the optoelectronic semiconductor CdZnTe, yielding important images of trap density distributions that may help elucidate the effects of optoelectronic traps and improve the quality and performance of photon detectors and photovoltaic devices fabricated on this type of a substrate.

AUTHOR INFORMATION

Corresponding Author

Andreas Mandelis − *Center for Advanced Diffusion-Wave and Photoacoustic Technologies, University of Toronto, Toronto, Ontario M5S 3G8, Canada; Institute for Advanced Non-Destructive and Non-Invasive Diagnostic Technologies (IANDIT), Toronto, Ontario M5S 3G8, Canada;* Email: mandelis@mie.utoronto.ca

Authors

Alexander Melnikov − *Center for Advanced Diffusion-Wave and Photoacoustic Technologies, University of Toronto, Toronto, Ontario M5S 3G8, Canada; Institute for Advanced Non-Destructive and Non-Invasive Diagnostic Technologies*

https://doi.org/10.1021/acsaelm.1c00100
ACS Appl. Electron. Mater. 2021, 3, 2551−2563

(IANDIT), Toronto, Ontario M5S 3G8, Canada; orcid.org/0000-0002-0020-9862

Akshit Soral − *Center for Advanced Diffusion-Wave and Photoacoustic Technologies, University of Toronto, Toronto, Ontario M5S 3G8, Canada*

Claudia Zavala-Lugo − *Center for Advanced Diffusion-Wave and Photoacoustic Technologies, University of Toronto, Toronto, Ontario M5S 3G8, Canada; Technical University of Queretaro (UTEQ), Queretaro 76130, Mexico*

Michal Pawlak − *Institute of Physics, Nicolaus Copernicus University, 87-100 Torun, Poland*

Complete contact information is available at: https://pubs.acs.org/10.1021/acsaelm.1c00100

Notes

The authors declare no competing financial interest.

■ ACKNOWLEDGMENTS

The authors are grateful to the Natural Sciences and Engineering Research Council of Canada (NSERC) for the Discovery Grant to A.M. and to the Canada Research Chairs Program. A.M. is grateful to CFI-ORF for the J. R. E. Leaders Fund (JELF) grant. They wish to thank K. S. and A. M. for support in sample preparation. M.P. thanks the National Science Centre Poland for grant no. 2015/19/D/ST3/02388.

■ REFERENCES

(1) Prokesch, M.; Soldner, S. A.; Sundaram, A. CdZnTe detectors for gamma spectrosocopy and x-ray photon counting at 250 × 10^6 photons/(mm^2s). *J. Appl. Phys.* **2018**, *124*, No. 044503.

(2) Del Sordo, S.; Abbene, L.; Caroli, E.; Mancini, A. M.; Zappettini, A.; Ubertaini, P. Progress in the Development of CdTe and CdZnTe Semiconductor Radiation Detectors for Astrophysical and Medical Applications. *Sensors* **2009**, *9*, 3491−3526.

(3) Takahashi, T.; Watanabe, S. Recent Progress in CdTe and CdZnTe Detectors. *IEEE Trans. Nucl. Sci.* **2001**, *48*, 950−959.

(4) Rezaie, N.; Kosarian, A. Efficiency improvement of CdZnTe solar cell by modification of interface layer. *Opt. Quantum Electron.* **2015**, *47*, 3237−3251.

(5) Zhou, C.; Chung, H.; Wang, X.; Bermel, P. Design of CdZnTe & Crystalline Silicon Tandem Junction Solar cells. *IEEE J. Photovoltaics* **2016**, *6*, 301−308.

(6) Gul, R.; Li, Z.; Rodriguez, R.; Keeter, K.; Bolotnikov, A.; James, R. In *Defect Measurements in CdZnTe Detectors Using I-DLTS, TCT, I-V, C-V and γ-ray Spectroscopy*, Proceeding SPIE 7079, Hard X-Ray, Gamma-Ray, and Neutron Detector Physics X, 70790U, SPIE, San Diego, California, 2008.

(7) Szeles, C. Advances in the Crystal Growth and Device Fabrication Technology of CdZnTe Room Temperature Radiation Detectors. *IEEE Trans. Nucl. Sci.* **2004**, *51*, 1242−1249.

(8) Strzałkowski, K. The composition effect on the thermal and optical properties across CdZnTe crystals. *J. Phys. D: Appl. Phys.* **2016**, *49*, No. 435106.

(9) Hsu, H. P.; Lin, D. Y.; Chen, C. W.; Wu, Y. F.; Strzałkowski, K.; Sitarek, P. Optical characterizations of $Cd_{1-X}Zn_XTe$ mixed crystals grown by vertical Bridgman-Stockbarger method. *J. Crystal Growth* **2020**, *534*, No. 125491.

(10) Mandelis, A.; Batista, J.; Shaughnessy, D. Infrared photocarrier radiometry of semiconductors: Physical principles, quantitative depth profilometry, and scanning imaging of deep subsurface electronic defects. *Phys. Rev. B* **2003**, *67*, No. 205208.

(11) Batista, J.; Mandelis, A.; Shaughnessy, D. Temperature dependence of carrier mobility in Si wafers measured by infrared photocarrier radiometry. *Appl. Phys. Lett.* **2003**, *82*, 4077−4079.

(12) Li, B.; Shaughnessy, D.; Mandelis, A.; Batista, J.; Garcia, J. Accuracy of photocarrier radiometric measurement of electronic transport properties of ion-implanted silicon wafers. *J. Appl. Phys.* **2004**, *96*, 186−196.

(13) Mandelis, A.; Pawlak, M.; Wang, C.; Delgadillo-Holtfort, I.; Pelzl, J. Time-domain and lock-in rate-window photocarrier radiometric measurements of recombination processes in silicon. *J. Appl. Phys.* **2005**, *98*, No. 123518.

(14) Shaughnessy, D.; Mandelis, A. Electronic Defect and Contamination Monitoring in Si Wafers Using Spectrally Integrated Room-Temperature Photo-Carrier Radiometry. *J. Electrochem. Soc.* **2006**, *153*, G283−G290.

(15) Melnikov, A.; Mandelis, A.; Tolev, J.; Lioudakis, E. Infrared photocarrier radiometry, modulated photovoltage and electrical characteristics of polycrystalline Si solar cell. *J. Phys.: Conf. Ser.* **2010**, *214*, No. 012111.

(16) Melnikov, A.; Mandelis, A.; Halliop, B.; Kherani, N. P. Interface state effects in hydrogenated amorphous-crystalline silicon heterostructures using UV laser photocarrier radiometry. *J. Appl. Phys.* **2013**, *114*, No. 244506.

(17) Zhang, Y.; Melnikov, A.; Mandelis, A.; Halliop, B.; Kherani, N. P.; Zhu, R. Optoelectronic transport properties in amorphous/crystalline silicon solar cell heterojunctions using frequency-domain photocarrier radiometry: Multi-parameter measurement reliability and precision studies. *Rev. Sci. Instrum.* **2015**, *86*, No. 033901.

(18) Mandelis, A.; Melnikov, A.; Tolev, J.; Xia, J.; Huq, S.; Lioudakis, E. Non-Destructive Infrared Optoelectronic Lock-in Carrierography of mc-Si Solar Cells. *Quant. Infrared Thermogr. J.* **2010**, *7*, 35−54.

(19) Sun, Q. M.; Melnikov, A.; Mandelis, A. Quantitative self-calibrating lock-in carrierographic lifetime imaging of silicon wafers. *Appl. Phys. Lett.* **2012**, *101*, No. 242107.

(20) Mandelis, A.; Zhang, Y.; Melnikov, A. Statistical theory and applications of lock-in carrierographic image pixel brightness dependence on multi-crystalline Si solar cell efficiency and photovoltage. *J. Appl. Phys.* **2012**, *112*, No. 054505.

(21) Liu, J.; Melnikov, A.; Mandelis, A. Silicon solar cell electrical parameter measurements through quantitative lock-in carrierographic (photoluminescence) and thermographic imaging. *Phys. Status Solidi A* **2013**, *210*, 2135−2145.

(22) Song, P.; Yang, F.; Liu, J.; Mandelis, A. Lock-in carrierography non-destructive imaging of silicon wafers and silicon solar cells. *J. Appl. Phys.* **2020**, *128*, No. 180903.

(23) Melnikov, A.; Chen, P.; Zhang, Y.; Mandelis, A. Lock-in and Heterodyne Carrierographic Imaging Characterization of Industrial Multicrystalline Silicon Solar Cells. *Int. J. Thermophys.* **2012**, *33*, 2095−2102.

(24) Sun, Q. M.; Melnikov, A.; Mandelis, A.; Pagliaro, R. Surface recombination velocity imaging of wet-cleaned silicon wafers using quantitative heterodyne lock-in carrierography. *Appl. Phys. Lett.* **2018**, *112*, No. 012105.

(25) Song, P.; Melnikov, A.; Sun, Q. M.; Mandelis, A.; Liu, J. Y. Uniqueness range optimization of photocarrier transport parameter measurements using combined quantitative heterodyne lock-in carrierography imaging and photocarrier radiometry. *J. Appl. Phys.* **2019**, *125*, No. 065701.

(26) Hu, L.; Mandelis, A.; Sun, Q. Ultrahigh-Frequency Heterodyne Lock-In Carrierography for Large-Scale Quantitative Multi-Parameter Imaging of Colloidal Quantum Dot Solar Cells. *IEEE J. Photovoltaics* **2019**, *9*, 132−138.

(27) Song, Y.; Mandelis, A.; Melnikov, A.; Sun, Q. An optoelectronic notch ('dip') phenomenon in the photocarrier radiometry frequency response of Si wafers: a route to quantitative trap-state dynamic processes in semiconductors. *Semicond. Sci. Technol.* **2020**, *35*, No. 115024.

(28) Xia, J.; Mandelis, A. Noncontact deep level photo-thermal spectroscopy: Technique and application to semi-insulating GaAs Wafers. *Appl. Phys. Lett.* **2007**, *90*, No. 062119.

(29) Mandelis, A.; Xia, J. Deep level photothermal spectroscopy: Physical principles and applications to semi-insulating GaAs band-gap multiple trap states. *J. Appl. Phys.* **2008**, *103*, No. 043704.

(30) Xia, J.; Mandelis, A. Broadening effects and ergodicity in deep level photothermal spectroscopy of defect states in semi-insulating GaAs: A combined temperature-, pulse-rate-, and time-domain study of defect state kinetics. *J. Appl. Phys.* **2009**, *105*, 103712.
(31) Sze, S. M.; Li, Y.; Ng, K. K. *Physics of Semiconductor Devices*; 2nd ed.; Wiley Interscience, New York, 1981; Vol. 2.
(32) Castaldini, A.; Cavallini, A.; Fraboni, B.; Fernandez, P.; Piqueras, J. Deep energy levels in CdTe and CdZnTe. *J. Appl. Phys.* **1998**, *83*, 2121−2126.
(33) Davis, C. B.; Allred, D. D.; Reyes-Mena, A.; Gonzalez-Hernandez, J.; Gonzalez, O.; Hess, B. C.; Allred, W. P. Photoluminescence and absorption studies of defects in CdTe and $Zn_xCd_{1-x}Te$ crystals. *Phys. Rev. B* **1993**, *47*, 13363−13369.
(34) Li, Y.; Zha, G.; Wei, D.; Yang, F.; Dong, J.; Xi, S.; Xu, L.; Jie, W. Effect of deep-level defects on the performance of CdZnTe photon counting detectors. *Sensors* **2020**, *20*, No. 2032.
(35) D'Errico, J. http://www.mathworks.com/matlabcentral/fileexchange/8277.
(36) Thomas, B.; Veale, M. C.; Wilson, M. D.; Seller, P.; Schneider, A.; Iniewski, K. Characterisation of Redlen high-flux CdZnTe. *J. Inst.* **2017**, *12*, No. C12045.
(37) Schlesinger, T. E.; Toney, J. E.; Yoon, H.; Lee, E. Y.; Brunett, B. A.; Franks, L.; James, R. B. Cadmium zinc telluride and its use as a nuclear radiation detector material. *Mater. Sci. Eng., R* **2001**, *32*, 103−189.
(38) McGregor, D.; Hermon, H. Room-temperature compound semiconductor radiation detectors. *Nucl. Instrum. Methods Phys. Res., Sect. A* **1997**, *395*, 101−124.

https://doi.org/10.1021/acsaelm.1c00100
ACS Appl. Electron. Mater. 2021, 3, 2551−2563